

Material Extrusion Additive Manufacturing of Lunar Soil Simulant Brick

Ailing Xun¹, Yingyu Chen¹, Lu Zhang^{1,2,*}, Chao Xu^{2,3,4}, Meng Zou², Luquan Ren²

¹College of Construction Engineering, Jilin University, Changchun 130026, China

²Key Laboratory of Bionic Engineering (Ministry of Education), Jilin University, Changchun 130025, China

³Institute of Structured and Architected Materials, Liaoning Academy of Materials, Shenyang 110167, China

⁴Weihai Institute for Bionics, Jilin University, Weihai 264207, China

*Correspondence Author

Abstract: *In-situ utilization of lunar soil resources to create construction units such as bricks is one of the best methods for establishing architectures on the moon, avoiding the exorbitant costs associated with transporting materials and massive equipment from Earth. In the paper, bricks with grid structures made of lunar soil simulants are fabricated via direct ink writing (DIW), a material extrusion additive manufacturing technique. The lunar soil simulant ink is prepared by mixing lunar soil simulant powders with polylactic acid (PLA)/dichloromethane (DCM) binder in a volume ratio of 74:26 and then extruded from a nozzle with a diameter of 410 μm to form cylindrical bricks following the preset printing path. The as-printed bricks are sintered under a vacuum condition at 1100 °C to enhance their mechanical properties. The sintered bricks exhibit dimensional shrinkages of around 10-15% due to PLA pyrolysis and sintering neck formation. Surprisingly, two of the sintered bricks display significantly greater mass loss ratios than the others, which may be due to gas generation from certain minerals during high-temperature sintering. This has been confirmed by microscopic analyses conducted on both the lunar soil simulant and fabricated bricks using scanning electron microscope (SEM), energy dispersive spectroscopy (EDS), and X-ray diffraction (XRD). The mechanical behaviors and failure modes of as-printed and sintered bricks are evaluated, showing compressive strengths of 5-6 MPa and 5-27 MPa, respectively. The elastic modulus and compressive strength of sintered bricks are positively correlated to their relative densities. In addition, bricks featuring mortise and tenon joint structures are also successfully manufactured, enabling direct jointing of different bricks without any binding material, which provides a novel approach to constructing lunar structural components.*

Keywords: Lunar soil simulant, Direct ink writing, Sintering, Mechanical properties.

1. Introduction

The moon, the nearest celestial body to Earth, harbors abundant resources (Crawford 2015). It serves as the primary destination for human space exploration, possessing immense potential for scientific discovery and technological advancement (Ehrenfreund et al. 2012, Hassanalian et al. 2018). The establishment of lunar infrastructure and permanent bases represents one of the next phases in human space exploration (Benaroya and Bemold 2008, Lee and van Riessen 2022, Pagnini et al. 2023). This monumental endeavor will pave the way for further advancements in our understanding of the universe. The construction of a lunar base necessitates significant quantities of building materials, and the transportation expenses associated with conveying these materials from Earth to the Moon are exorbitant (Duke et al. 2003). Therefore, In-Situ Resource Utilization (ISRU) is widely regarded as the optimal approach for lunar surface construction (Isachenkov et al. 2021, Wang et al. 2022). However, a major challenge in this field lies in the need for practical approaches to enable outposts and settlements to sustain themselves through ISRU and optimized resource recycling (Santomartino et al. 2023). In addition, the lunar environment is considerably more hostile than that of Earth (Zhou et al. 2019). Other challenges associated with ISRU for lunar surface construction include vacuum conditions, microgravity effects, extreme temperatures, seismic activities, etc. Therefore, further studies into ISRU on the Moon are imperative.

Lunar soil is the most abundant and easily accessible ISRU material. Over the past decade, scientists and researchers have attempted to utilize additive manufacturing (AM), also known

as 3D printing, to fabricate lunar soil simulants into large or small components and structures. Leach et al. (2012) discussed the potential use of contour crafting (CC) in constructing lunar surface infrastructure, including roads, landing pads, habitat platforms, walls, and dome structures, using locally sourced lunar soil. The CC technique uses a computer-controlled nozzle to extrude lunar concrete in layers without molds, followed by trowels to smooth out the outer surface. Cesaretti et al. (2014) employed the D-shape technique to fabricate large components for the lunar outpost by spraying liquid binding solutions onto the surface of a mixture of lunar soil simulant and MgO powders with mobile nozzles. The lunar soil simulant powders are consolidated via the chemical reaction of MgO and binder, with this process being repeated for each subsequent layer until a large component is achieved. Although these techniques have demonstrated their capability in printing large-scale structures on Earth, they are not the optimal choices for lunar surface construction due to the high volatility of the liquid binder and the instability of interlayer bonding effects in low gravity and ultra-high vacuum environments. Moreover, the equipment of the large-scale AM technique is excessively bulky, which would significantly increase transportation costs between Earth and the Moon. Therefore, other scholars focused on using lunar soil simulant to fabricate small-scale components possessing specific mechanical properties via AM.

Krishna Balla et al. (2012) first attempted to use lunar soil simulant with particle sizes ranging from 50 to 150 μm as raw materials to fabricate dense solid cylinders of 8-10 mm in diameter and 25-30 mm in height via Laser Engineering Net Shaping (LENSTM). Lunar soil simulant powders are dispersed on the substrate and then synchronously melted by

the laser beam. The molten materials rapidly cool and solidify, gradually forming a near-net shape part according to the printing path. Goulas et al. (2019) demonstrated the potential of laser selective melting (SLM), a powder-bed fusion technique, for fabricating complex structures using lunar soil simulant powders under 125 μm . They also conducted mechanical tests on 5mm cubic structures with relative porosities of 44-49% and densities of 1.76-2.3 g/cm^3 , showing their compressive strengths between 0.2 and 4.2 MPa, comparable to the minimum compressive strength for standard masonry clay bricks (3.5 MPa). However, these powder-based AM techniques involve using dispersed soil particles, which are easy to float under low gravity, resulting in the difficulty of controlling the printing process, thus reducing the mechanical properties of the components. These floating particles may also damage the printer, disrupting printing. Liu et al. (2018) fabricated millimeter-sized dovetail blocks, bolts and nuts, and rectangular structures (21.6mm \times 4mm \times 2.5mm) using digital light processing (DLP) and subsequent sintering. The printing slurries were prepared by mixing photocurable resins with grinded lunar soil simulant powders in ratios of 55-45 vol%, and the resins pyrolyze after sintering. The resulting nearly dense samples exhibit maximum compressive and bending strengths of 428 and 130 MPa, respectively. However, the liquid-based 3d printing technique requires a substantial amount of resin and incurs high transportation costs. Additionally, the impact of low gravity on its printing process remains a significant challenge for its practical application in the lunar environment. Direct Ink Writing (DIW) is a material extrusion (MEX) AM technique, which extrudes lunar soil ink through high-precision printing needles and stacks layer by layer to form a three-dimensional structure. Then the overall structure is heated, and lunar soil powders are sintered into a ceramic structure (Jakus et al. 2017, Taylor et al. 2017). In light of the technology using pressure extrusion, low gravity has less impact on the printing process.

In this paper, small structural components, i.e., cylindrical lunar soil simulant bricks and bricks with mortise and tenon joint structures, are fabricated via DIW and subsequent sintering. The lunar soil simulant ink is prepared by blending lunar soil simulant powders and the binder. The DIW printing parameters are adjusted to achieve successful fabrication of lunar soil simulant bricks. The subsequent sintering is carried out in a vacuum atmosphere to improve its mechanical properties. The microstructural and mechanical properties of lunar soil simulant bricks are characterized by scanning electron microscopy (SEM), energy dispersive spectroscopy (EDS), and X-ray diffraction (XRD) analyses, as well as compression tests.

2. Materials and Methods

2.1 Materials

The inks used in the fabrication of lunar soil simulant bricks were synthesized by blending 74 vol.% lunar soil simulant and 26 vol.% binder. The lunar soil simulant was provided by China Aerospace Science and Technology Corporation (CASC), mainly composed of plagioclase, olivine, and pyroxene, with a particle density of 2.74 g/cm^3 measured by pycnometer test. Figure 1 illustrates the grain size distribution

(GSD) curves of the lunar soil simulant and Apollo series lunar soil. Compared with the actual lunar soil, the GSD of the lunar soil simulant closely approximates the upper limit of Apollo series lunar soil. The lunar soil simulant used in the study was selected through sieving to ensure its particle size was below 75 μm , thereby preventing any potential nozzle obstruction during printing. The SEM (Zeiss Sigma300) image of the post-sieved lunar soil simulant in Figure 2 shows irregularly shaped and unevenly sized particles with sharp edges, which closely resemble the morphology of actual lunar soil particles. The binder was formulated by mixing polylactic acid (PLA) and dichloromethane (DCM) in a volume ratio of 1:4, with DCM serving as a solvent to dissolve PLA. The binder was left at ambient temperature for 24 hours until it achieved homogeneity before use.

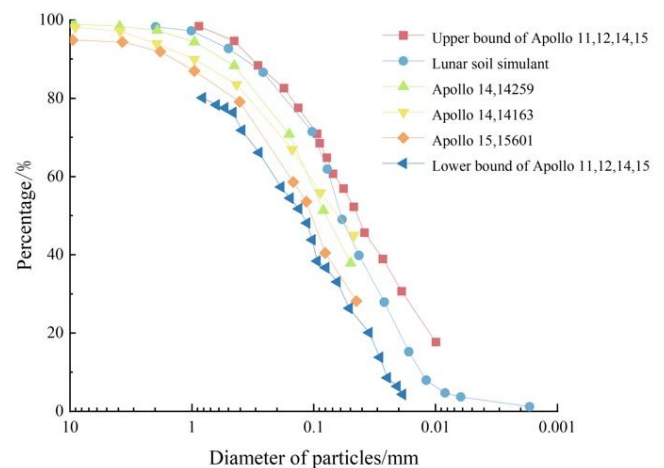


Figure 1: GSD curves of lunar soil simulant and Apollo series lunar soils

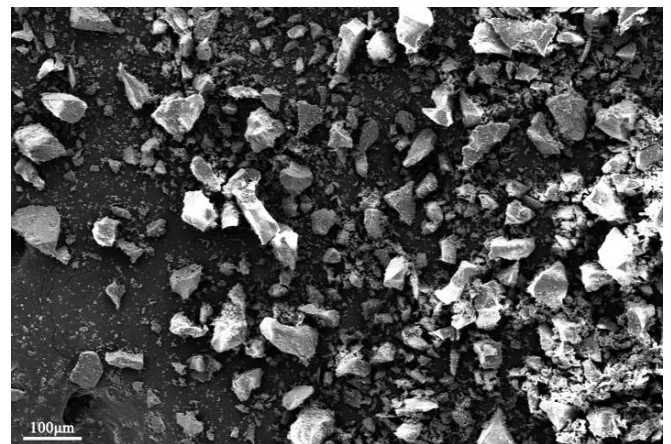


Figure 2: SEM image of lunar soil simulant

2.2 Methods

2.2.1 DIW and sintering of lunar soil simulant bricks

The lunar soil simulant ink was homogenized using an XQM-2L ball mill for one hour and promptly transferred into a syringe to prevent ink solidification caused by the high volatility of DCM, which may impede subsequent printing. The ink-filled syringe was equipped with a nozzle featuring an inner tip diameter of 410 μm and then inserted into a DIW 3D printer (AEP-2) for printing at an extrusion speed of 8-9 mm/s and an extrusion pressure between 200 and 240 kPa. The layer height and filling percentage were set at 0.31mm and 60%, respectively.

The ink was extruded through the syringe nozzle to form a filament, which was subsequently deposited layer by layer while DCM in the ink evaporated immediately after extrusion. After each layer was printed, the deposition direction was altered by 90°, and the next layer was added until a cylindrical brick structure with a diameter of 10mm and height of 20mm had been fabricated.

The as-printed brick was subsequently sintered in a KTL1700 vacuum tube furnace. The temperature was elevated from ambient to 1000 °C at a rate of 5 °C /min, during which PLA underwent pyrolysis at approximately 300 °C, followed by a slower increase from 1000 °C to 1100 °C at a rate of 1.6 °C /min, and ultimately held at 1100°C for four hours to facilitate sintering neck formation between lunar soil simulant particles. The sintered bricks were retrieved from the furnace once the temperature had naturally subsided to ambient levels.

2.2.2 Microstructural and mechanical characterizations of lunar soil simulant bricks

The dimensions and masses of the as-printed and sintered cylindrical bricks were measured by a vernier caliper and balance, respectively, based on which their shrinkages and relative densities were calculated using the equation (Taylor et al. 2018),

$$RD = \rho_b / \rho_s \quad (1)$$

where ρ_b is the density of the brick, ρ_s is the density of the lunar soil simulant, taken as 2.74 g/cm³, and ρ_b is calculated based on the mass and total volume measured with a balance and caliper, respectively.

Sintered bricks were labeled as RD-1 and RD-2 according to their different relative densities, with RD-1 exhibiting a higher relative density than RD-2. The RD-1 and RD-2 bricks were sectioned radially to display their cross-sectional profiles. After being polished with sandpaper, the cross sections were imaged using SEM to reveal the microscopic structures. The chemical compositions were analyzed via EDS (Oxford AZtecLive and Ultim Max) at an accelerating voltage of 5 kV.

The sintered bricks were ground into powders using a mortar and pestle and subjected to an XRD (XRD-6100) analysis at 40 kV voltage and 30 mA current to determine their mineral phases. The incident angle and diffraction speed were set at 5° and 4°/min, respectively. Additionally, the XRD analysis of raw lunar soil simulant particles were carried out for comparison with the sintered lunar soil simulant.

Three as-printed brick samples (A-1, A-2, and A-3) and five sintered brick samples (S-1, S-2, S-3, S-4, and S-5) were conducted with compression tests using a UTM8104 electronic universal testing machine at a displacement rate of 1 mm/min until complete fracture occurred. The elastic modulus and compression strength were determined by the compressive stress-strain curves. The failure morphologies were documented through photography. The compressive properties of as-printed and sintered brick samples were then compared. Furthermore, the influence of the relative density of the sintered brick samples on their compressive strength

was quantified.

3. Result and Discussion

3.1 Shrinkage and Mass Loss Analyses of Sintered Lunar Soil Simulant Bricks

The optical images of as-printed and sintered lunar soil simulant bricks are presented in Figure 3a. The former appears dark gray, while the latter is slightly darker with subtle differences between them, both resembling the color of raw lunar soil simulant powders. The as-printed brick exhibits a uniform arrangement of filaments and a regular cylindrical shape, free from defects. Upon sintering, the brick retains its original geometry but undergoes slight dimensional shrinkage due to PLA pyrolysis and the formation of sintering necks between lunar soil simulant particles. Figure 3b presents a sample of sintered bricks with mortise and tenon joint structures inspired by ancient Chinese wooden buildings, allowing direct jointing of different bricks instead of using binding material.

Table 1 shows the dimension, mass, shrinkage ratio, and relative density of as-printed and sintered lunar soil simulant bricks. After sintering, the samples shrunk in all three dimensions (X, Y, and Z). The X and Y axes exhibited a similar shrinkage ratio at approximately 10- 12%, while the Z axis experienced a slightly higher rate of around 11-15%. The dimension shrinkage of lunar soil simulant bricks is caused by PLA pyrolysis and the formation of sintering necks between lunar soil simulant particles. The PLA pyrolysis leads to a loss in the mass of sintered bricks. Due to the gravitational influence of Earth, greater shrinkage ratios are observed along the Z-axis for these bricks. Compared to the shrinkage ratio, a relatively more expansive range of variation in mass loss ratio is observed between as-printed and sintered masses of lunar soil simulant brick, ranging from 7.14% to 32.43%. Figure 4 illustrates the dimension shrinkage and mass loss ratios of the five lunar soil simulant bricks. As the dimension shrinkage ratio decreases for the first three bricks, there is a corresponding reduction in their mass loss ratio. S-3 exhibits the least mass loss ratio, consistent with its slightest dimensional shrinkage ratios. While the shrinkage ratios of S-4 and S-5 are comparable to those of S-1 and S-2, their mass loss ratios are approximately two times greater than those of S-1 and S-2. The results suggest that the mass loss of S-4 and S-5 is not solely attributed to PLA pyrolysis. The low-melting-point solid constituents or of the lunar soil simulant particles in S-4 and S-5 may evaporate under vacuum conditions (Song Lei et al. 2018), resulting in gas generation that causes pressure buildup within the filament structure of bricks, hindering their dimensional shrinkage and rendering them similar in size to S-1, S-2, and S-3. The difference in relative density among sintered lunar soil simulant bricks reflects the variation in pore development within lunar soil simulant bricks. S-4 and S-5 exhibit lower relative densities than the others due to their significant mass loss during sintering, indicating the presence of more internal pores within the filaments resulting from evaporation of low-melting-point solids or gas formation under a vacuum atmosphere. The SEM images of sintered bricks will be provided in the following section to reinforce the discussion.

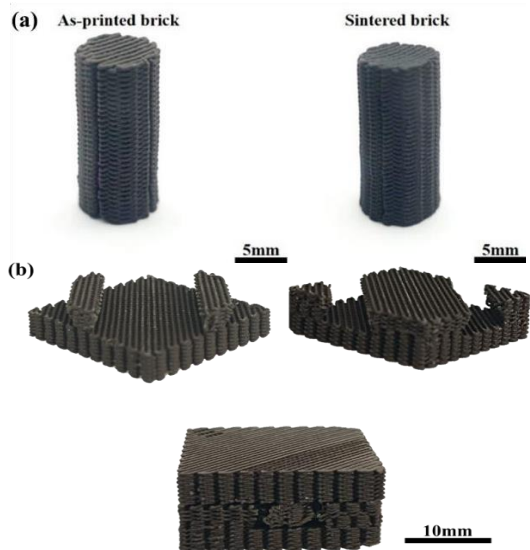


Figure 3: Optical images of as-printed and sintered lunar soil simulant bricks

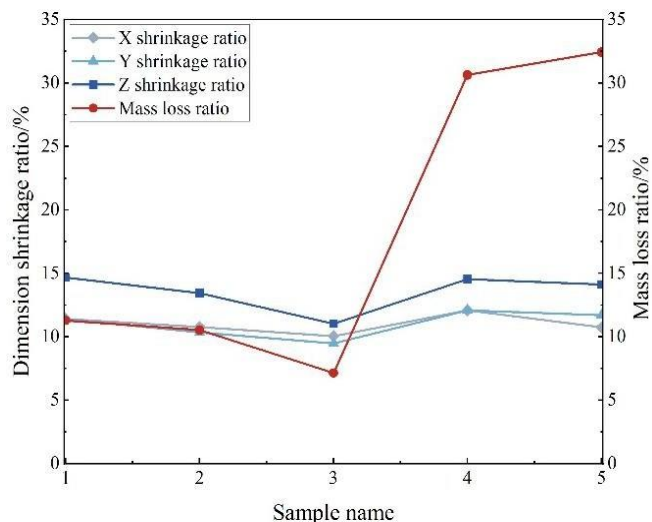


Figure 4: Relationships between mass loss and dimension shrinkage ratios

Table 1: Shrinkage and mass parameters of as-printed and sintered lunar soil simulant bricks

sample name	as-printed dimension			sintered dimension			shrinkage ratio		as-printed mass	sintered mass	mass loss	relative density
	mm			mm			%					
	x	y	z	x	y	z	x	z	g	g	%	--
S-1	8.87	8.96	19.50	7.86	7.94	16.64	11.40	14.67	1.33	1.18	11.28	0.53
S-2	8.91	8.99	19.86	7.95	8.06	17.19	10.77	13.44	1.33	1.19	10.53	0.50
S-3	8.86	8.97	19.67	7.97	8.12	17.50	10.05	11.03	1.26	1.17	7.14	0.48
S-4	8.52	8.60	19.79	7.49	7.56	16.91	12.09	14.55	1.11	0.77	30.63	0.37
S-5	8.56	8.72	19.69	7.64	7.70	16.90	11.70	14.12	1.11	0.75	32.43	0.35

3.2 Microstructural Analysis of Lunar Soil Simulant Bricks

Figure 5 displays SEM images of two sintered lunar soil simulant bricks, namely RD-1 with a high relative density of 0.51 and RD-2 with a low relative density of 0.39, captured at different magnifications. Their pore structures are significantly different. The filaments of RD-1 are well-formed and regularly arranged after sintering, as shown in Figures 5a and b. Filaments across different layers are sintered together, and the structural pores between adjacent filaments are well retained while in-filament pores are presented due to PLA pyrolysis. Figures e and f illustrate the microstructure of RD-2, which indicates that more pores are generated inside the filament due to both PLA pyrolysis and gas generation, which then expand from inside to the outside of the filament to connect with the structural pores and produce larger pores compared to RD-1, thereby affecting the forming quality of the printed lunar soil simulant brick structure. Both the

magnified images of RD-1 (Figures 5c and d) and RD-2 filaments (Figures 5g and h) show the formation of sintering necks between irregular lunar soil simulant particles, providing specific strengths for the structure.

To further elucidate the causes of mass loss and large pore formation in RD-2, EDS and XRD analyses were carried out to compare the chemical and mineral compositions of the sintered brick with those of raw lunar soil simulant powders. Figure 6 shows the atomic percentages of chemical elements present in the lunar soil simulant before and after sintering. The lunar soil simulant comprises a variety of chemical elements, including carbon, oxygen, silicon, aluminum, iron, calcium, etc. Among these elements, oxygen has the highest content, followed by carbon. Additionally, a significant carbon reduction is observed after sintering the brick, which indicates that the primary volatile component produced during this process is carbon.

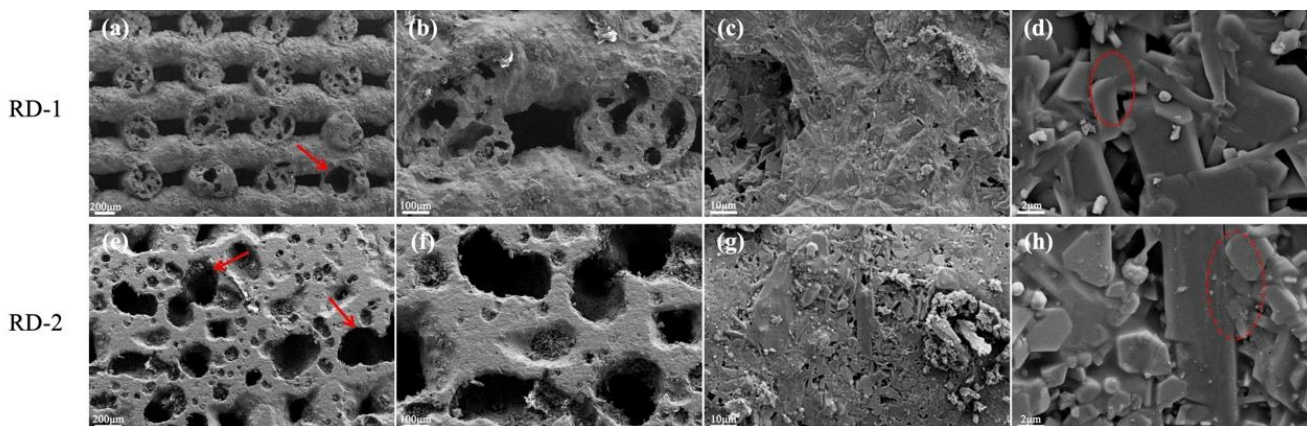


Figure 5: SEM images of lunar soil simulant sintered sample with high and low relative densities

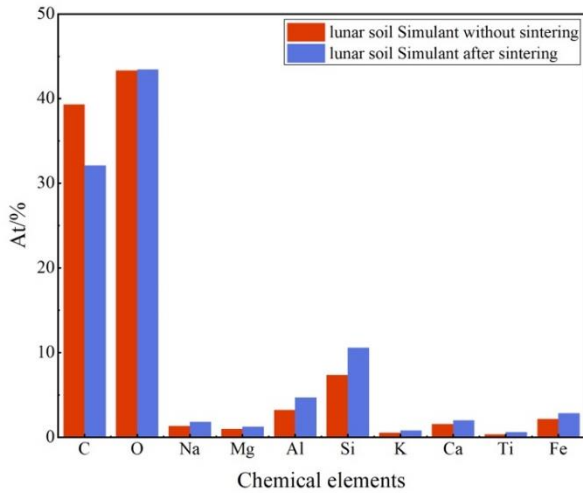


Figure 6: Chemical composition of lunar soil simulant before and after sintering

The XRD spectra presented in Figure 7 illustrate the mineral phases of raw and sintered lunar soil simulant powders. The discrepancy between all phases before and after sintering is the variation in peak intensities. Plagioclase, olivine, pyroxene, and dolomite are the primary components of the raw powders prior to sintering. However, the dolomite phase is no longer detectable in the spectrum after undergoing sintering processes due to its instability at high temperatures, which leads to decomposition into carbon dioxide gas (Wang et al. 2014). The overflow of carbon from the sintered lunar soil simulant results in a decrease in carbon content and the formation of numerous pores within the filaments, consistent with the discussion mentioned above. Moreover, the XRD spectra reveal the presence of magnetite, hematite, and ilmenite phases present after sintering, with very low peak intensities for hematite and ilmenite. This could be attributed to either the compositional disparity of the tested samples or the slight oxidation of iron at high temperatures during sintering. If it is for the latter reason, introducing an inert gas such as nitrogen or argon into the furnace can further enhance the vacuum atmosphere and prevent oxidation. In addition, high-temperature pyrolysis of olivine may occur, causing the reaction between magnesium olivine with silicon dioxide and resulting in the formation of the pyroxene phase. This phenomenon accounts for the increased intensity of pyroxene phases in the XRD spectrum of sintered lunar soil simulant.

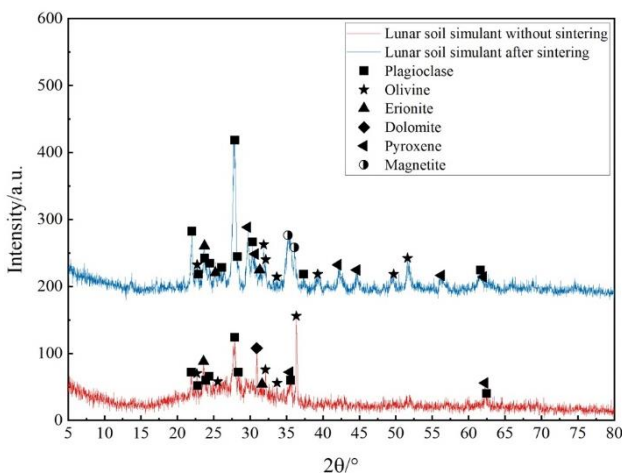


Figure 7: XRD spectra of lunar soil simulant before and after sintering.

3.3 Compressive Properties of Sintered Lunar Soil Simulant Bricks

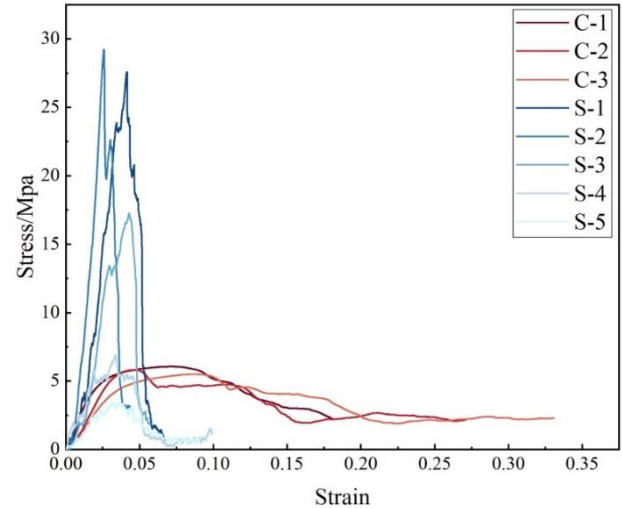


Figure 8: Compressive stress-strain curves of as-printed and sintered lunar soil simulant bricks.

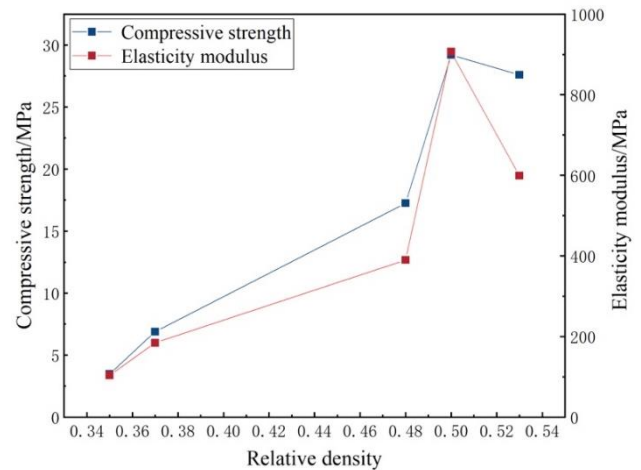


Figure 9: Failure images of as-printed and sintered lunar soil simulant bricks during compression tests.

The compressive stress-strain curves for three as-printed and five sintered lunar soil simulant bricks are depicted in Figure 8, while their failure images during compression tests are presented in Figure 9. Figure 8 illustrates the plastic softening stages of the as-printed samples A-1, A-2, and A-3 under compression, demonstrating plastic failure with compressive strengths ranging from approximately 5 to 6 MPa. Furthermore, Figures 9a, b, and c show that the failure modes of the as-printed bricks mainly comprise shear failure along the top and tensile failure of the entire brick in the horizontal direction under compressive stress. When the internal structure of the sample is homogeneous, it tends to undergo shear failure under compression. The occurrence of flat tensile failure is due to the interconnectivity between unsintered particles via the binder. Under compressive stress, these filaments are prone to plastic deformation and flattening, leading to changes in the overall structure and weakened connections in the horizontal direction that ultimately result in tensile failure. These two types of failure can be utilized to assess the homogeneity and plastic deformation tendency of as-printed bricks under compressive stress.

Differently, the sintered bricks display an obvious brittle

failure mode under compression tests, exhibiting compressive strengths ranging from approximately 5 to 27 MPa. Among them, the compressive strength of S-4 and S-5 is comparable to the experimental results obtained by Jakus et al. (2017) under a hydrogen atmosphere, while S-1, S-2, and S-3 show superior compressive properties. The stress-strain curve of S-2 exhibits the highest slope values in its linear part and peak compressive stress, indicating that it possesses superior elastic modulus and compressive strength compared to other sintered bricks. This suggests that the overall load-bearing capability of the sintered brick is fully realized. While the stress-strain curves of S-4 and S-5 exhibit their low elastic moduli and compressive strengths, indicating multiple occurrences of cracking and damage during compression, ultimately leading to the premature failure of their load-bearing capability. In Figures 9d and e, S-1 and S-2 exhibit the mode of shear failure, indicating their homogeneous internal structures and complete load-bearing abilities. The shear plane of S-1 traverses the entire brick, while that of S-2 is located in the lower left corner, only intersecting with half of the brick. The rest of S-2 continues to bear a certain level of loading, which explains the occurrence of its secondary peak value in Figure 8. During compression, S-4 and S-5 gradually develop cracks and collapse into fragments (as shown in Figures 9g and h),

indicating the presence of concentrated pores within the bricks, leading to stress concentration and weak planes that ultimately fail along these planes and insufficient overall strength. Figure 9f reveals that the S-3 brick exhibits a failure mode characterized by a combination of shear failure and fragment collapse, with its compressive strength falling between those associated with shear and fragmentation.

The correlation between the mechanical properties (elastic modulus and compressive strength) of sintered bricks and their corresponding relative density is illustrated in Figure 10. Both compressive strength and elastic modulus increase with the rise of relative density.

By integrating the analysis of the SEM images in Figure 5, it can be inferred that the pore structure plays a crucial role in determining the mechanical behavior of lunar soil simulant bricks. When the internal pores are fewer and evenly distributed, the mechanical properties of lunar soil simulant bricks exhibit superiority. However, if numerous in-filament pores emerge and connect with structural pores to form cracks, the sintered bricks may fail along these cracks and result in a significant decrease in elastic modulus and compressive strength.

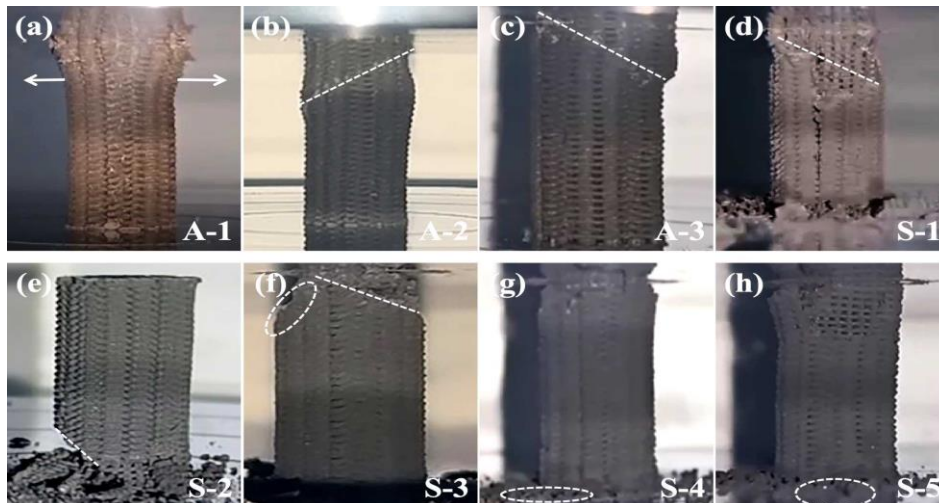


Figure 10: Correlation between mechanical properties and relative density of sintered lunar soil simulant bricks

4. Conclusion

The lunar soil simulant ink was formulated by mixing lunar soil simulant powders and PLA/DCM binder at a volumetric ratio of 74%. Porous cylindrical bricks and bricks with mortise and tenon joint structures were successfully fabricated using the formulated ink via DIW, a MEX technique that is less affected by low gravity on the Moon than other AM methods. Subsequent sintering in a vacuum atmosphere was carried on the as-printed bricks to improve their mechanical properties, miming the vacuum condition on the lunar surface. The as-printed and sintered bricks exhibit uniformly arranged filaments and regularly shaped structural pores without any defects. Sintering caused 10-12% and 11-15% shrinkage in the radial and longitudinal directions of the bricks, respectively. This is due to PLA pyrolysis and the formation of sintering necks between lunar soil simulant particles, which also results in the presence of in-filament pores and mass loss in sintered bricks. Therefore, the mass loss ratio should be positively correlated to the shrinkage ratio, verified by the results for sintered bricks S-1, S-2, and S-3. However, the

sintered bricks S-4 and S-5 show significantly greater mass loss ratio and larger number of in-filament pores than the others due to the decomposition of dolomite into the gas overflow of carbon dioxide at high sintering temperatures, demonstrated by the SEM, EDS, and XRD analyses. In addition, compressive strength, elastic modulus, and failure mode of as-printed and sintered lunar soil simulant bricks were compared, indicating shear and tensile failures for the former and shear and fragmentation for the latter. The sintered bricks possess superior mechanical properties (maximum compressive strength of 27 MPa) compared to the as-printed bricks (maximum compressive strength of 6 MPa). However, their load-bearing capacity is hindered by the formation of in-filament pores and interconnectivity between in-filament and structural pores. Additionally, the compressive strength and elastic modulus of the sintered brick are positively correlated to its relative density. To further enhance the mechanical property of sintered bricks, future research should focus on preventing large pore formations that generate weak planes by secondary infiltration or adjustment of sintering parameters.

References

- [1] Benaroya, H. and Bernold, L. 2008. Engineering of lunar bases, *Acta Astronautica*, 62(4): 277–299. doi:10.1016/j.actaastro.2007.05.001.
- [2] Cesaretti, G. Dini, E. De Kestelier, X. Colla, V. and Pambaguian, L. 2014. Building components for an outpost on the Lunar soil by means of a novel 3D printing technology, *Acta Astronautica*, 93: 430–450. doi:10.1016/j.actaastro.2013.07.034.
- [3] Crawford, I.A. 2015. Lunar resources: A review, *Progress in Physical Geography: Earth and Environment*, 39(2): 137–167. doi:10.1177/0309133314567585.
- [4] Duke, M.B. Blair, B.R. and Diaz, J. 2003. Lunar resource utilization: Implications for commerce and exploration, *Advances in Space Research*, 31(11): 2413–2419. doi:10.1016/S0273-1177(03)00550-7.
- [5] Ehrenfreund, P. McKay, C. Rummel, J.D. Foing, B.H. Neal, C.R. Masson-Zwaan, T. Ansdell, M. Peter, N. Zarnecki, J. Mackwell, S. Perino, M.A. Billings, L. Mankins, J. and Race, M. 2012. Toward a global space exploration program: A stepping stone approach, *Advances in Space Research*, 49(1): 2–48. doi:10.1016/j.asr.2011.09.014.
- [6] Goulas, A. Binner, J.G. Engstrøm, D.S. Harris, R.A. and Friel, R.J. 2019. Mechanical behaviour of additively manufactured lunar regolith simulant components, *Proceedings of the Institution of Mechanical Engineers, Part L: Journal of Materials: Design and Applications*, 233(8): 1629–1644. doi:10.1177/1464420718777932.
- [7] Hassanalian, M. Rice, D. and Abdelkefi, A. 2018. Evolution of space drones for planetary exploration: A review, *Progress in Aerospace Sciences*, 97: 61–105. doi:10.1016/j.paerosci.2018.01.003.
- [8] Isachenkov, M. Chugunov, S. Akhatov, I. and Shishkovsky, I. 2021. Regolith-based additive manufacturing for sustainable development of lunar infrastructure – An overview, *Acta Astronautica*, 180: 650–678. doi:10.1016/j.actaastro.2021.01.005.
- [9] Jakus, A.E. Koube, K.D. Geisendorfer, N.R. and Shah, R.N. 2017. Robust and Elastic Lunar and Martian Structures from 3D-Printed Regolith Inks, *Scientific Reports*, 7(1): 44931. Nature Publishing Group. doi:10.1038/srep44931.
- [10] Kobaka, J. Katzer, J. and Zarzycki, P.K. 2019. Pilbara Craton Soil as A Possible Lunar Soil Simulant for Civil Engineering Applications, *Materials*, 12(23): 3871. doi:10.3390/ma12233871.
- [11] Krishna Balla, V. Roberson, L.B. O'Connor, G.W. Trigwell, S. Bose, S. and Bandyopadhyay, A. 2012. First demonstration on direct laser fabrication of lunar regolith parts, *Rapid Prototyping Journal*, 18(6): 451–457. Emerald Group Publishing Limited. doi:10.1108/13552541211271992.
- [12] Leach, N. Carlson, A. Khoshnevis, B. and Thangavelu, M. 2012. Robotic Construction by Contour Crafting: The Case of Lunar Construction, *International Journal of Architectural Computing*, 10(3): 423–438. doi:10.1260/1478-0771.10.3.423.
- [13] Lee, S. and Van Riessen, A. 2022. A Review on Geopolymer Technology for Lunar Base Construction, *Materials*, 15(13): 4516. doi:10.3390/ma15134516.
- [14] Liu, M. Tang, W. Duan, W. Li, S. Dou, R. Wang, G. Liu, B. and Wang, L. 2019. Digital light processing of lunar regolith structures with high mechanical properties, *Ceramics International*, 45(5): 5829–5836. doi:10.1016/j.ceramint.2018.12.049.
- [15] Pagnini, F. Manzey, D. Rosnet, E. Ferravante, D. White, O. and Smith, N. 2023. Human behavior and performance in deep space exploration: next challenges and research gaps, *npj Microgravity*, 9(1): 1–7. Nature Publishing Group. doi:10.1038/s41526-023-00270-7.
- [16] Santomartino, R. Aversch, N.J.H. Bhuiyan, M. Cockell, C.S. Colangelo, J. Gumulya, Y. Lehner, B. Lopez-Ayala, I. McMahan, S. Mohanty, A. Santa Maria, S.R. Urbaniak, C. Volger, R. Yang, J. and Zea, L. 2023. Toward sustainable space exploration: a roadmap for harnessing the power of microorganisms, *Nature Communications*, 14(1): 1391. Nature Publishing Group. doi:10.1038/s41467-023-37070-2.
- [17] Song, L. Xu, J. Fan, S. Tang, H. Li, X. Liu, J. and Duan, X. 2019. Vacuum sintered lunar regolith simulant: Pore-forming and thermal conductivity, *Ceramics International*, 45(3): 3627–3633. doi:10.1016/j.ceramint.2018.11.023.
- [18] Taylor, S.L. Jakus, A.E. Koube, K.D. Ibeh, A.J. Geisendorfer, N.R. Shah, R.N. and Dunand, D.C. 2018. Sintering of micro-trusses created by extrusion-3D-printing of lunar regolith inks, *Acta Astronautica*, 143: 1–8. doi:10.1016/j.actaastro.2017.11.005.
- [19] Wang, F. Kuzuya, T. Hirai, S. Li, J. and Li, T. 2014. Carbon Dioxide Absorption and Release Properties of Pyrolysis Products of Dolomite Calcined in Vacuum Atmosphere, *The Scientific World Journal*, 2014: 1–7. doi:10.1155/2014/862762.
- [20] Wang, Y. Hao, L. Li, Y. Sun, Q. Sun, M. Huang, Y. Li, Z. Tang, D. Wang, Y. and Xiao, L. 2022. In-situ utilization of regolith resource and future exploration of additive manufacturing for lunar/martian habitats: A review, *Applied Clay Science*, 229: 106673. doi:10.1016/j.clay.2022.106673.
- [21] Zhou, C. Chen, R. Xu, J. Ding, L. Luo, H. Fan, J. Chen, E.J. Cai, L. and Tang, B. 2019. In-situ construction method for lunar habitation: Chinese Super Mason, *Automation in Construction*, 104: 66–79. doi:10.1016/j.autcon.2019.03.024.
- [22] Zhou, S. Lu, C. Zhu, X. and Li, F. 2021. Preparation and Characterization of High-Strength Geopolymer Based on BH-1 Lunar Soil Simulant with Low Alkali Content, *Engineering*, 7(11): 1631–1645. doi:10.1016/j.eng.2020.10.016.